

A male mouse model for metabolic dysfunction-associated steatotic liver disease and hepatocellular carcinoma

Received: 28 October 2023

Accepted: 16 July 2024

Published online: 02 August 2024

 Check for updates

Byung-Kwan Jeong ^{1,2,8}, Won-Il Choi ^{1,2,8}, Wonsuk Choi^{3,8} , Jieun Moon^{1,2}, Won Hee Lee^{1,2}, Chan Choi⁴, In Young Choi⁵, Sang-Hyun Lee⁵, Jung Kuk Kim ⁵, Young Seok Ju ^{1,2}, Pilhan Kim ^{1,2}, Young-Ah Moon⁶, Jun Yong Park ⁷  & Hail Kim ^{1,2} 

The lack of an appropriate preclinical model of metabolic dysfunction-associated steatotic liver disease (MASLD) that recapitulates the whole disease spectrum impedes exploration of disease pathophysiology and the development of effective treatment strategies. Here, we develop a mouse model (Streptozotocin with high-fat diet, STZ + HFD) that gradually develops fatty liver, metabolic dysfunction-associated steatohepatitis (MASH), hepatic fibrosis, and hepatocellular carcinoma (HCC) in the context of metabolic dysfunction. The hepatic transcriptomic features of STZ + HFD mice closely reflect those of patients with obesity accompanying type 2 diabetes mellitus, MASH, and MASLD-related HCC. Dietary changes and tirzepatide administration alleviate MASH, hepatic fibrosis, and hepatic tumorigenesis in STZ + HFD mice. In conclusion, a murine model recapitulating the main histopathologic, transcriptomic, and metabolic alterations observed in MASLD patients is successfully established.

Metabolic dysfunction-associated steatotic liver disease (MASLD) encompasses a range of disorders characterized by excessive accumulation of triglyceride (TG) in hepatocytes, replacing the previous term non-alcoholic fatty liver disease (NAFLD), which relies on exclusionary confounder terms¹. MASLD progresses from TG accumulation (metabolic dysfunction-associated steatotic liver, MASL) to inflammation and hepatocellular injury (metabolic dysfunction-associated steatohepatitis, MASH), hepatic fibrosis, and, ultimately, cirrhosis and/or hepatocellular carcinoma (HCC)². MASLD is a rapidly growing health concern³ that has made an increasing contribution to end-stage liver disease in recent years, thus imposing a substantial socioeconomic burden^{4–6}. Owing to the lack of suitable MASLD animal models, limited

studies have focused on the exploration of the underlying mechanisms and treatment strategies⁷. Therefore, establishment of an animal model that adequately reflects the entire spectrum of MASLD remains a crucial unmet need.

Patients with metabolic disorders, such as type 2 diabetes mellitus (T2DM) and obesity, have a higher prevalence of MASLD and exacerbated risk of developing MASH, advanced fibrosis (defined as fibrosis stage ≥ 3), and HCC^{8–10}. In a recent study on T2DM patients who had undergone liver biopsies, MASH and advanced fibrosis were detected in 58% and 38% cases, respectively¹¹. Another study reported a higher incidence of MASLD and advanced fibrosis in T2DM patients with obesity compared to those without¹². However, the mechanism

¹Graduate School of Medical Science and Engineering, KAIST, Daejeon 34141, Korea. ²Biomedical Research Center, KAIST, Daejeon, Korea. ³Department of Internal Medicine, Chonnam National University Hwasun Hospital, Chonnam National University Medical School, Hwasun, Korea. ⁴Department of Pathology, Chonnam National University Medical School, Hwasun, Korea. ⁵Hanmi Research Center, Hanmi Pharmaceutical Co. Ltd, Hwaseong, Korea. ⁶Department of Molecular Medicine, Inha University College of Medicine, Incheon 22212, Korea. ⁷Department of Internal Medicine, Yonsei University College of Medicine, Yonsei Liver Center, Severance Hospital, Seoul, Korea. ⁸These authors contributed equally: Byung-Kwan Jeong, Won-Il Choi, Wonsuk Choi.

 e-mail: wonsuc1@uci.edu; drpjy@yuhs.ac; hailkim@kaist.edu

underlying the rapid progression of MASLD in individuals with T2DM and obesity is not well understood.

From the therapeutic aspect, pharmacological interventions based on lifestyle may be effective in blocking pathological progression in T2DM patients with obesity, since MASLD develops rapidly in this population¹³. Tirzepatide, a dual glucose-dependent insulinotropic polypeptide/glucagon-like peptide-1 receptor agonist (GIP/GLP-1 RA), is a commonly used therapeutic agent for both T2DM and obesity^{14–16}, with clinically proven efficacy against MASL¹⁷. However, the issue of whether continuous use of tirzepatide can prevent the development of advanced fibrosis or HCC remains to be resolved. Furthermore, there is a paucity of evidence regarding the optimal time to administer tirzepatide across the broad spectrum of MASLD.

In this study, we developed a mouse model of MASLD encompassing the whole spectrum of the disease, including MASL, MASH, advanced fibrosis, and HCC. The model was generated by treatment with low-dose streptozotocin (STZ) in conjunction with a high-fat diet (HFD) and utilized to demonstrate the therapeutic efficacy of tirzepatide against MASH, fibrosis, and HCC.

Results

HFD exposure after low-dose STZ administration induces the whole spectrum of MASLD in mice

To generate an animal model of MASLD that mimics the pathophysiological alterations in human patients, we administered low-dose STZ to 7-week-old C57BL/6j male mice, followed by either standard chow diet (SCD) (STZ + SCD) or HFD (STZ + HFD) for 6–60 weeks from 8 weeks of age (Supplementary Fig. 1a). The hepatic phenotype of STZ + HFD mice was initially examined. Notably, these mice developed hepatomegaly and a creamy color change attributable to TG accumulation after 14 weeks of age, followed by grossly visible hepatic tumors after 38 weeks (Fig. 1a–c). Moreover, STZ + HFD mice exhibited sequential histological changes of MASLD from MASL to MASH, hepatic fibrosis, and HCC (Fig. 1d, e). The NAFLD activity score (NAS) had increased sufficiently by 20 weeks of age to diagnose MASH. Perivenular/pericellular hepatic fibrosis developed starting from 20 weeks and progressed to significant fibrosis (defined as fibrosis stage ≥ 2) by 32 weeks of age. By 44 weeks, the majority of mice had progressed to advanced fibrosis, with one exhibiting cirrhosis (Fig. 1f, g and Supplementary Fig. 1b–d). Plasma aspartate aminotransferase (AST) and alanine aminotransferase (ALT) levels were elevated (Fig. 1h, i). Consistently, intravital liver imaging quantification of hepatic lipid droplets and collagen fibers revealed progressive development of hepatic steatosis and fibrosis in STZ + HFD mice (Fig. 1j–l). From 20 weeks of age, STZ + HFD mice showed an increase in the apoptotic cell content in the liver, which was significantly elevated at 32 weeks of age (Supplementary Fig. 1e). In addition, STZ + HFD mice developed grossly evident hepatic tumors as early as 38 weeks of age, with a gradual increase in the incidence and number of tumors by 68 weeks (Fig. 1m, n).

Next, we compared the metabolic phenotypes of mice in the STZ + HFD and STZ + SCD treatment groups to determine whether MASLD progression occurred in the context of metabolic dysfunction, similar to that observed in humans¹⁸. Compared to STZ + SCD mice, the STZ + HFD group showed increased body weight gain, fat mass, fasting glucose and insulin levels, homeostatic model assessment for insulin resistance (HOMA-IR), visceral adipocyte hypertrophy and inflammation, and plasma lipid levels (Supplementary Fig. 1f–p).

Mice without STZ treatment were also fed SCD (SCD-only) or HFD (HFD-only) from 8 weeks of age and compared with STZ + HFD mice. Hepatic inflammation and hepatocyte ballooning were less increased in HFD-only mice compared to STZ + HFD mice at 20 and 32 weeks of age (Supplementary Fig. 2a–f). STZ + HFD mice also showed more fibrosis compared to HFD-only mice at 32 weeks of age (Supplementary Fig. 2g, h). No advanced stage fibrosis or hepatic tumor were

observed in HFD-only mice until 50 weeks of age (Supplementary Fig. 3a–k). Regarding the metabolic phenotypes, STZ + HFD mice demonstrated a lesser increase in fat mass and body weight compared to HFD-only mice but manifested a rapid increase in fasting blood glucose levels and glucose intolerance at 20 weeks of age (Supplementary Fig. 4a–e). Overall, the STZ + HFD mouse model clearly exhibited the whole disease spectrum of MASLD (Fig. 1o).

Molecular characteristics of MASH progression in STZ + HFD mice

To identify molecular changes occurring during MASH progression, we performed RNA-seq with liver samples from STZ + HFD mice at various stages. The hepatic transcriptome changed gradually until 32 weeks of age and became more heterogeneous after tumorigenesis (Fig. 2a). Based on transcriptomic changes, 4 groups of genes were clustered (Fig. 2b). During MASH progression, groups of genes related to fatty acid metabolism and cell cycle transition (C1) were gradually upregulated, while those related to cholesterol synthesis and liver function (C2) were gradually downregulated (Fig. 2b–d). In mice at 32 weeks of age, genes involved in fibrosis and PI3K-Akt signaling pathways (C4) showed abrupt upregulation, while those involved in amino acid catabolism (C3) showed abrupt downregulation (Fig. 2b–d). Differentially expressed genes (DEGs) between mice aged 32 weeks and those aged 14 to 20 weeks were similar to genes belonging to the groups that underwent abrupt changes in expression at 32 weeks (C3, C4) (Fig. 2e). The hepatic transcriptomic alterations occurring throughout MASH progression in STZ + HFD mice are summarized in Fig. 2f.

MASH developed rapidly and extensively in 20- and 32-week-old STZ + HFD mice (Supplementary Fig. 2b–h). Accordingly, we further examined the hepatic transcriptomic and epigenetic phenotypes of mice in SCD-only, STZ + SCD, HFD-only, and STZ + HFD treatment groups at 20 weeks of age to gain insights into the mechanisms underlying the rapid progression of MASH. In hepatic transcriptome analysis, three distinct gene clusters were identified among the four groups (Supplementary Fig. 5a, b). Cluster A genes were involved in tissue repair processes (such as cell cycle proliferation, inflammatory response, and fibrosis) and downregulated in STZ + HFD mice compared to HFD-only mice (Supplementary Fig. 5c–f). Assay for transposase accessible chromatin sequencing (ATAC-seq) analysis revealed significant alterations in the chromatin landscape of STZ + HFD mice relative to other mouse groups (Supplementary Fig. 5g, h). STZ + HFD mice exhibited widespread epigenetic repression, which was mainly associated with responses to DNA damage and misfolded protein (Supplementary Fig. 5i, j). In line with epigenetic changes, mRNA expression of genes related to homologous DNA repair was downregulated in STZ + HFD mice compared to HFD-only mice (Supplementary Fig. 5k). Next, we examined the hepatic transcriptomic phenotypes of mice in SCD-only, STZ + SCD, HFD-only, and STZ + HFD treatment groups at 32 weeks of age. Cluster E genes, related to Wnt and Notch signaling, and the cell cycle pathway were upregulated in STZ + HFD mice compared to HFD-only mice (Supplementary Fig. 6a–f). These findings suggest that loss of compensatory responses against metabolic dysfunction is the main driver of rapid MASH progression in STZ + HFD mice. Additionally, signaling pathways related to hepatic carcinogenesis are upregulated before hepatic tumor development in these mice.

To ascertain whether the molecular characteristics of MASH progression in STZ + HFD mice reflect the etiology of MASH in humans, RNA-seq was performed on liver tissues from 28 MASLD patients and 4 healthy liver transplantation donors (Supplementary Table 1) and compared to the hepatic transcriptome of STZ + HFD mice. A significant correlation was observed between patients with NAS 2–6 and fibrosis stage 0–1 and STZ + HFD mice at 14 to 20 weeks of age and between patients with NAS 4–7 and fibrosis stage 4 and STZ + HFD mice

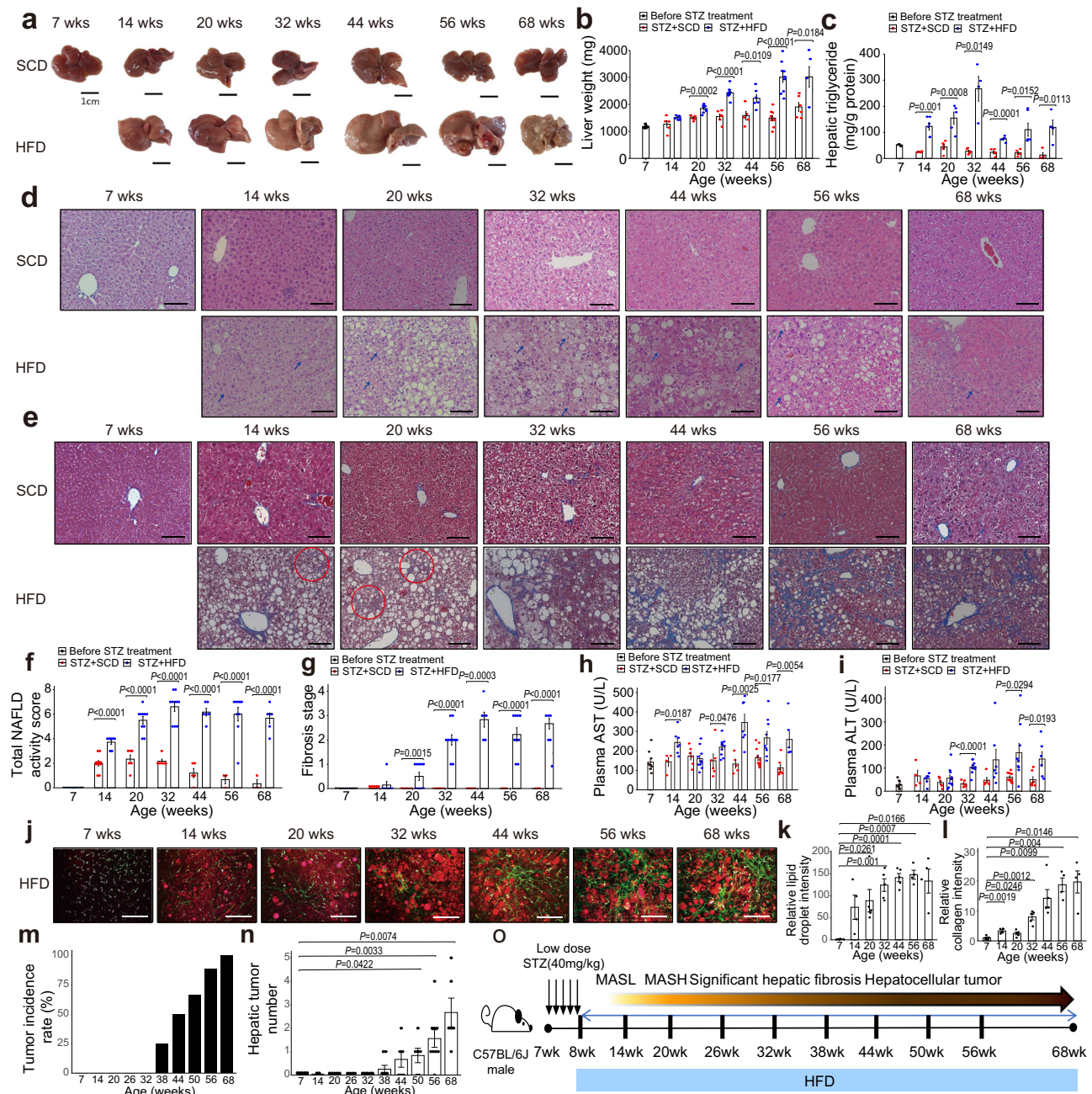


Fig. 1 | HFD feeding after STZ administration induces the whole spectrum of MASLD. a–n Seven-week-old B6J mice were treated with STZ and fed SCD (STZ + SCD) or HFD (STZ + HFD) for 6–60 weeks. **a** Representative liver gross image of STZ-treated mice. Scale bar, 1 cm. **b** Liver weight; Before STZ treatment, $n = 10$; STZ + SCD, $n = 5, 6, 6, 5, 10$, and 6 , from 14 to 68-week-old, respectively; STZ + HFD, $n = 7, 9, 9, 6, 9$, and 5 , from 14 to 68-week-old, respectively. **c** Hepatic triglyceride levels; Before STZ treatment, $n = 4$; STZ + SCD, $n = 4, 6, 6, 5, 5$, and 4 , from 14 to 68-week-old, respectively; STZ + HFD, $n = 6, 5, 4, 5, 6$, and 4 , from 14 to 68-week-old, respectively. Representative liver histology evaluated via **(d)** H&E staining and **(e)** Masson's trichrome staining for hepatic fibrosis in STZ-treated mice. Blue arrows indicate ballooning degeneration of hepatocytes. Red circles signify perisinusoidal fibrosis. The data are representative results of the biological replicates shown in **f** and **g**. Scale bar, 100 μm . **f, g** Nonalcoholic fatty liver disease score (NAS) and fibrosis stage graded using the NASH CRN scoring system in STZ-treated mice; Before STZ treatment, $n = 10$; STZ + SCD, $n = 10, 6, 6, 5, 3$, and 3 , from 14 to 68-week-

old, respectively; STZ + HFD, $n = 7, 10, 10, 6, 9$, and 6 , from 14 to 68-week-old, respectively. Plasma **(h)** AST and **(i)** ALT levels; Before STZ treatment, $n = 10$; STZ + SCD, $n = 10, 6, 6, 5, 5$, and 6 , from 14 to 68-week-old, respectively; STZ + HFD, $n = 7, 10, 10, 6, 9$, and 6 , from 14 to 68-week-old, respectively. Scale bar, 100 μm . **j–l** Hepatic lipid droplets (red, **k**) and collagen fibrils (green, **l**) of STZ + HFD mice assessed via *in vivo* liver imaging; $n = 5, 4, 5, 5, 4, 4$, from 7 to 68-week-old, respectively. Hepatic tumor **(m)** incidence and **(n)** number in STZ + HFD mice; $n = 10, 7, 10, 8, 10, 8, 6, 6, 9$, and 6 , from 7 to 68-week-old, respectively. **o** Comprehensive MASLD progression overview. Data are expressed as means \pm SEM. $^*P < 0.05$, $^{**}P < 0.01$, $^{***}P < 0.001$, $^{****}P < 0.0001$, compared with the age-matched group, Student's *t*-test or Welch's *t*-test (**b, c, and f–i**). $^{\#}P < 0.05$, $^{\#\#}P < 0.01$, $^{\#\#\#}P < 0.001$, $^{\#\#\#\#}P < 0.0001$, compared with the 7-week-old control group, two-sided Student's *t*-test or Welch's *t*-test (**b, c, f–l, k, l, n**). Source data are provided as a Source Data file.

Histopathological and molecular characteristics of hepatic tumors in STZ + HFD mice

We further assessed the histopathological features of hepatic tumors that developed in STZ + HFD mice. The majority of hepatic tumors developing from STZ + HFD mice occurred in non-cirrhotic liver with steatohepatic background, with an average NAS of 5.7 and an average fibrosis stage of 2.5 (Supplementary Table 2). Two major types of hepatic tumors were identified. One type showed a brightly colored, well-demarcated gross appearance with ballooning tumor cells, inflammatory cell infiltration, and mild nuclear atypia, comparable to steatohepatic HCC (Fig. 3a–c)^{20–22}. The other type was dark brownish in color, necrotic, and had a trabecular growth pattern with nuclear pleomorphisms, similar to conventional HCC (Fig. 3d–f)²³. To further confirm the malignant properties of tumors developing in STZ + HFD mice, immunohistochemical (IHC) staining was conducted²⁴. Among steatohepatic tumors, some showed reticulin loss in intra-tumoral sinusoid cells similar to HCC, while the others retained reticulin networks similar to hepatocellular adenoma (HCA) (Fig. 3g, k). Regardless of reticulin loss, all steatohepatic tumors were focally positive for glutamine synthase (GS) and glypican-3 (GPC-3) and displayed intra-tumor pericellular fibrosis (Fig. 3h–j, l–n). On the other hand, all conventional type tumors showed reticulin loss in intra-tumoral sinusoid cells, and their tumor cells were diffusely positive for GS and focally positive for GPC-3 (Fig. 3o–r). Taken together, the data indicate that hepatic tumors in STZ + HFD mice resemble the histopathological characteristics of HCC prevalent in MASLD patients²⁰.

To clarify the relevant molecular pathways of hepatic tumorigenesis in STZ + HFD mice, we performed RNA-seq of tumor and non-tumor tissues. Notably, the transcriptomes of tumor and non-tumor tissues showed significant differences (Supplementary Fig. 7a, b). In tumor tissues, genes related to cell cycle proliferation and HCC markers (*Glul* and *Gpc3*) were upregulated while those related to amino acid catabolism and oxidative phosphorylation were downregulated (Supplementary Fig. 7c–f). Based on the histopathological and molecular features, tumors were categorized into three groups (Fig. 3s, t, Supplementary Fig. 7g–k and Supplementary Table 3). Group 1 contained relatively small tumors that resembled premalignant lesions, such as HCA, according to their steatohepatic histology, retained reticulin networks, and paucity of transcriptome alterations compared to non-tumor tissue. Group 2 displayed tumors with steatohepatic histology, loss of reticulin network, and increased expression of genes involved in steroid biosynthesis (*Sreb2*, *Hmgcr*, and *Hmgcs1*), resembling steatohepatic HCC. Group 3 included tumors with trabecular growth patterns, severe nuclear pleomorphism, and increased expression of Wnt pathway genes (*Axin2*, *Ctnnb1*, and *Wnt5a*) that corresponded to conventional HCC.

To examine the association between known molecular subtypes in human HCC and hepatic tumor groups in STZ + HFD mice, gene set enrichment analysis (GSEA) was performed (Supplementary Fig. 8a)^{25–27}. Group 1 showed similarity to periportal-type HCC, well-known for good differentiation, while Group 2 was associated to Boyault's G1 and G2 subclasses, known for a high proliferation rate and poor prognosis^{25,27}. Group 3 exhibited similarities to CTNNB1 mutation-associated subtypes, including Boyault's G6 subclass, Hoshida's S2 subclass, and peri-venous type HCC^{25–27}. The frequency of group 2 and 3 tumors among the histologically identifiable hepatic tumors in STZ + HFD mice increased with age (Supplementary Fig. 8b). Furthermore, comparison of STZ + HFD mice tumor transcriptomes with public transcriptome data of MASLD-related HCC patients (GSE164760) demonstrated that tumors in Groups 2 and 3 had a higher likelihood of correlation with tumor tissues from patients with MASLD-related HCC (Fig. 3u)²⁸. On the other hand, Group 1 tumors of STZ + HFD mice displayed a significant correlation with those of MASH patients with cirrhosis and non-tumor adjacent

tissues obtained from MASLD-related HCC patients²⁸. To ascertain whether hepatic tumors developing in STZ + HFD mice specifically reflect MASLD-related HCC, transcriptome data from viral or alcoholic hepatitis patients with or without HCC (GSE 63898) were compared with STZ + HFD mice (Fig. 3v)²⁹. Notably, only Group 3 tumors showed a significant correlation with HCC of other etiologies. In addition, a comparison of the hepatic transcriptomes of diethylnitrosamine-treated HFD-fed mice (CRA000931) to those of MASLD-related HCC patients revealed no significant association (Supplementary Fig. 8c)³⁰. The collective findings clearly demonstrate that the developing hepatic tumors in STZ + HFD mice precisely recapitulate the histopathological and molecular characteristics of MASLD-related HCC.

Dietary changes effectively ameliorate MASH, hepatic fibrosis, and hepatic tumorigenesis in STZ + HFD mice

Lifestyle intervention, including weight loss, is a cornerstone of therapeutic management for MASLD¹³. From a therapeutic viewpoint, we investigated the stage of MASLD that could be potentially improved by lifestyle intervention in our model. To explore the effect of lifestyle intervention in MASH development, the diet of STZ + HFD mice was replaced at 20 weeks of age to SCD for 6 weeks (HFD → SCD 26 wk; Fig. 4a). Compared to STZ + HFD mice, HFD → SCD 26 wk mice showed amelioration of NAS and hepatic TG but no significant differences in hepatic fibrosis stage (Fig. 4b–g and Supplementary Fig. 9a–c). Transcriptomic analysis revealed that molecular alterations during MASH progression including fibrogenesis in STZ + HFD mice were partially reversed in HFD → SCD 26 wk mice (Fig. 4h, Supplementary Fig. 9d, e, and Supplementary tables 4, 5). While body weight was decreased in HFD → SCD 26 wk mice, fasting glucose and insulin levels and HOMA-IR were not significantly different from STZ + HFD mice (Supplementary Fig. 9f–i).

Next, to investigate the effect of dietary changes in the late stage of MASLD including significant fibrosis and HCC development, we replaced the diet of STZ + HFD mice at 33 weeks of age to SCD for 18 weeks (HFD → SCD 51 wk mice) (Fig. 4i). Compared to the STZ + HFD group, HFD → SCD 51 wk mice showed attenuated liver weight, hepatic TG, NAS, hepatic fibrosis, and incidence and number of hepatic tumors (Fig. 4j–r and Supplementary Fig. 9j–l). Similar to the data obtained with HFD → SCD 26 wk mice, transcriptomic changes during MASH progression in STZ + HFD mice were partly reversed in HFD → SCD 51 wk mice (Fig. 4s, Supplementary Fig. 9m, n, and Supplementary table 6, 7). Although body weight was reduced in HFD → SCD 51 wk mice, we observed no significant differences in fasting glucose and insulin levels and HOMA-IR relative to STZ + HFD mice (Supplementary Fig. 9o–r). Additionally, in HFD → SCD 51 wk mice, the majority of the genes related to gluconeogenesis or glycogenolysis remained unaltered, and the relevant pathways were not enriched in GSEA (Supplementary Fig. 9s, t, and Supplementary tables 6, 7). Our collective findings indicate that the dietary change from HFD to SCD could effectively mitigate MASH, hepatic fibrosis, and hepatic tumorigenesis in STZ + HFD mice.

Tirzepatide ameliorates MASH, hepatic fibrosis, and hepatic tumorigenesis in STZ + HFD mice

We further evaluated the therapeutic potential of tirzepatide, a dual GIP/GLP-1 RA, against various stages of MASH in STZ + HFD mice. To this end, STZ + HFD mice were administered vehicle or tirzepatide for 10 to 11 weeks at three different stages of MASH, beginning at 21 weeks (21–32 wk), 28 weeks (28–38 wk), and 41 weeks (41–52 wk) of age (Fig. 5a). Tirzepatide attenuated liver weight in 21–32 wk, 28–38 wk, and 41–52 wk treatment groups, NAS and hepatic fibrosis in 21–32 wk and 28–38 wk treatment groups (Fig. 5b–f and Supplementary Fig. 10a–c). In addition, in the tirzepatide treatment groups, no hepatic tumors were detected in the 28–38 wk treatment group, while hepatic

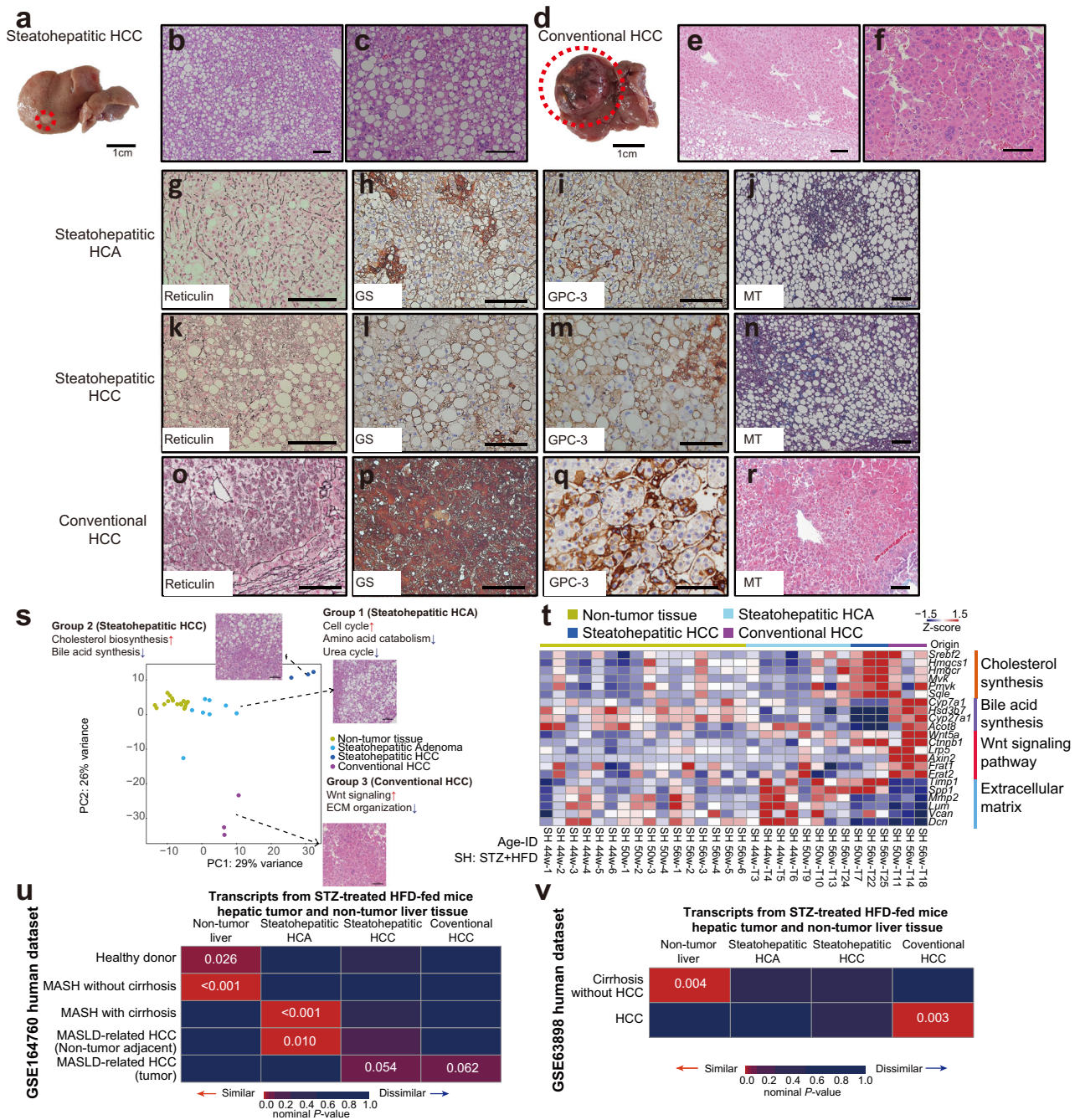


Fig. 3 | Histopathological and molecular characteristics of hepatic tumors in STZ + HFD mice. **a–n** Hepatic tumors originating from STZ + HFD mice resembling human steatohepatic hepatocellular carcinoma (HCC) (**a–c**, **k–n**), steatohepatic hepatocellular adenoma (HCA) (**g–j**), or conventional HCC (**d–f**, **o–r**). Representative (**a**) gross and (**b**, **c**) microscopic H&E images of hepatic tumor resembling steatohepatic HCC (Scale bar: **a**: 1 cm, **b**, **c**: 100 μ m). The red circle indicates tumor. The data are representative of 6 independent biological replicates. Representative (**d**) gross and (**e**, **f**) microscopic images of hepatic tumor resembling conventional HCC (Scale bar: **d**: 1 cm, **e**, **f**: 100 μ m). The red circle indicates tumor. The data are representative of 8 independent biological replicates. Immunohistochemical and histochemical staining of hepatic tumor resembling (**g–j**) steatohepatic HCA, (**k–n**) steatohepatic HCC, or (**o–r**) conventional HCC

(**g**, **k**, **o**; Reticulin, **h**, **l**, **p**; Glutamine synthase (GS), **i**, **m**, **q**; Glypican-3 (GPC-3), **j**, **n**, **r**; Masson’s trichrome (MT), scale bar: 100 μ m). The data are representative of (**g–j**) 11, (**k–n**) 6, or (**o–r**) 8 independent biological replicates. **s–v** Hepatic tumor and non-tumor liver tissues of 44 to 56-week-old STZ + HFD mice subjected to RNA-seq. **s** Principal component analyses of RNA-seq data, along with representative H&E images of different tumor groups (Scale bar: 100 μ m). **t** Heatmap displaying the top differentially enriched pathways in different tumor groups. **u** Submap clustering analyses with Fisher’s exact test comparing RNA-seq data of hepatic tumor and non-tumor liver tissues from STZ + HFD mice and human MASLD-related HCC patients (GSE164760). **v** Submap clustering analyses with Fisher’s exact test comparing RNA-seq data of hepatic tumor and non-tumor liver tissues from STZ + HFD mice and human HCC patients with viral or alcoholic hepatitis (GSE63898).

tumorigenesis was significantly decreased in 41–52 wk treatment group (Fig. 5g–i). In transcriptomic analysis, tirzepatide partially rescued the molecular alterations that developed with the progression of MASH in STZ + HFD mice, including upregulation of fatty acid

degradation, cell cycle, and gluconeogenesis pathways and downregulation of the ribosome pathway, while changes related to fibrosis were limited at the earlier stages (21–32 wk and 28–38 wk) (Fig. 5j–l). In addition, tirzepatide downregulated the genes related to Wnt

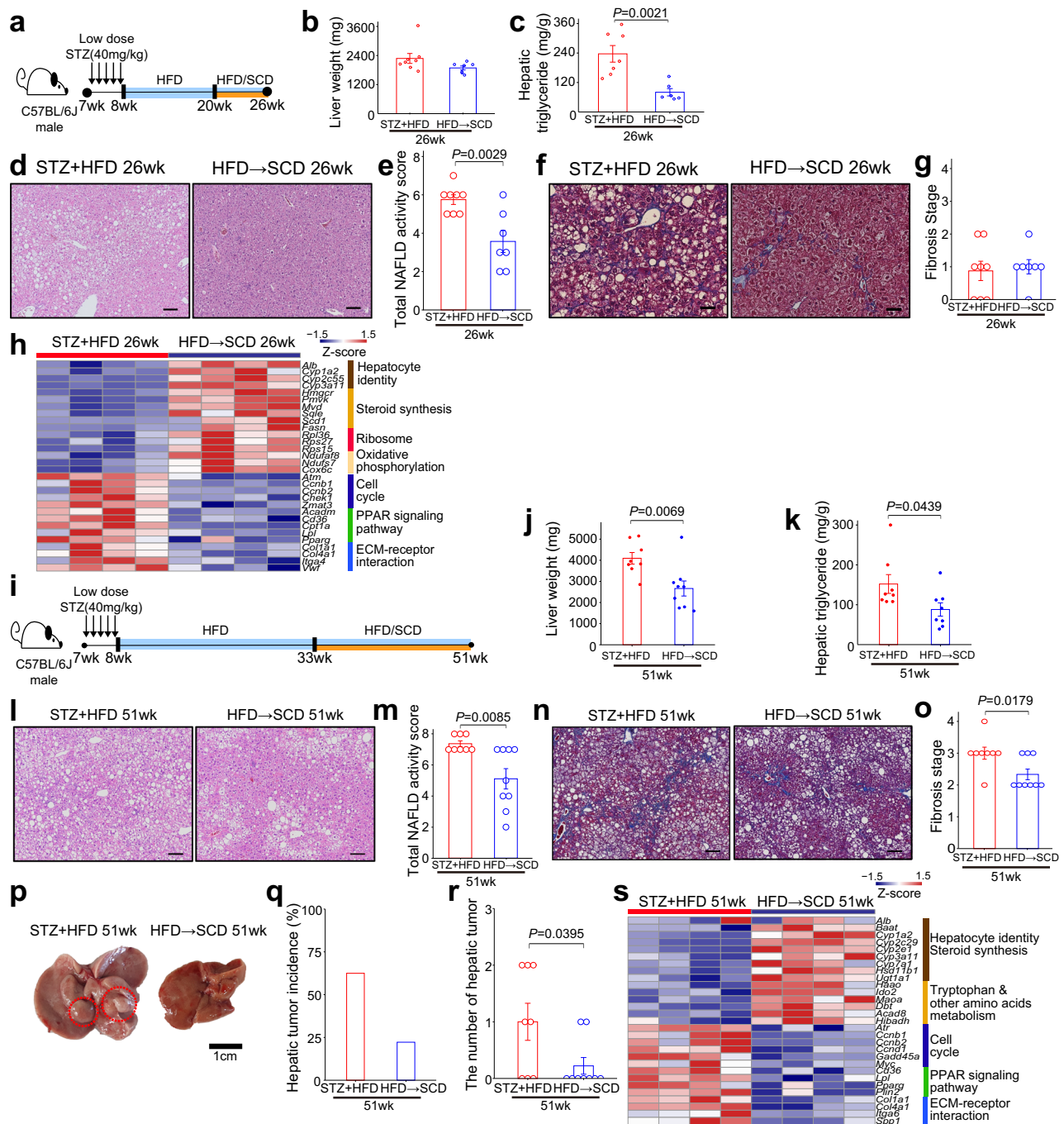


Fig. 4 | Dietary changes ameliorate MASH, hepatic fibrosis, and hepatic tumorigenesis in STZ + HFD mice. a–h Seven-week-old B6J mice were treated with STZ, fed HFD from 8 to 20 weeks, followed by HFD or SCD (HFD → SCD) until 26 weeks. **a** Schematic figure. **b** Liver weight; STZ + HFD, $n=8$; HFD → SCD, $n=7$. **c** Hepatic triglyceride levels; STZ + HFD, $n=7$; HFD → SCD, $n=6$. **d** Representative liver histology assessed via H&E staining (scale bar, 100 μ m). **e** NAS grading using the NASH CRN scoring system; STZ + HFD, $n=8$; HFD → SCD, $n=7$. **f** Representative liver histology with Masson's trichrome staining (scale bar, 100 μ m). **g** Fibrosis stage grading with the NASH CRN scoring system; STZ + HFD, $n=8$; HFD → SCD, $n=7$. **h** Heatmap displaying the top differentially enriched pathways between two groups. **i–s** Seven-week-old B6J mice were treated with STZ and fed HFD from 8 to 33 weeks, followed by administration of HFD or SCD (HFD → SCD) until 51 weeks.

i Schematic figure. **j** Liver weight; STZ + HFD, $n=8$; HFD → SCD, $n=9$. **k** Hepatic triglyceride levels; $n=8$ per group. **l** Representative liver histology evaluation via H&E staining (Scale bar, 100 μ m). **m** NAS grading based on the NASH CRN scoring system; STZ + HFD, $n=8$; HFD → SCD, $n=9$. **n** Representative liver histology via Masson's trichrome staining (Scale bar, 100 μ m). **o** Fibrosis stage grading via the NASH CRN scoring system; STZ + HFD, $n=8$; HFD → SCD, $n=9$. **p** Representative liver gross image (Scale bar, 1 cm). Red circles indicate hepatic tumors. Hepatic tumor **(q)** incidence and **(r)** number; STZ + HFD, $n=8$; HFD → SCD, $n=9$. **s** Heatmap displaying top differentially enriched pathways between two groups. Data are expressed as means \pm SEM. $P < 0.05$, $^{**}P < 0.01$, $^{***}P < 0.001$, $^{****}P < 0.0001$, compared with age-matched group, two-sided Student's *t*-test or Welch's *t*-test (**b**, **c**, **e**, **g**, **j**, **k**, **m**, **o**, **r**). Source data are provided as a Source Data file.

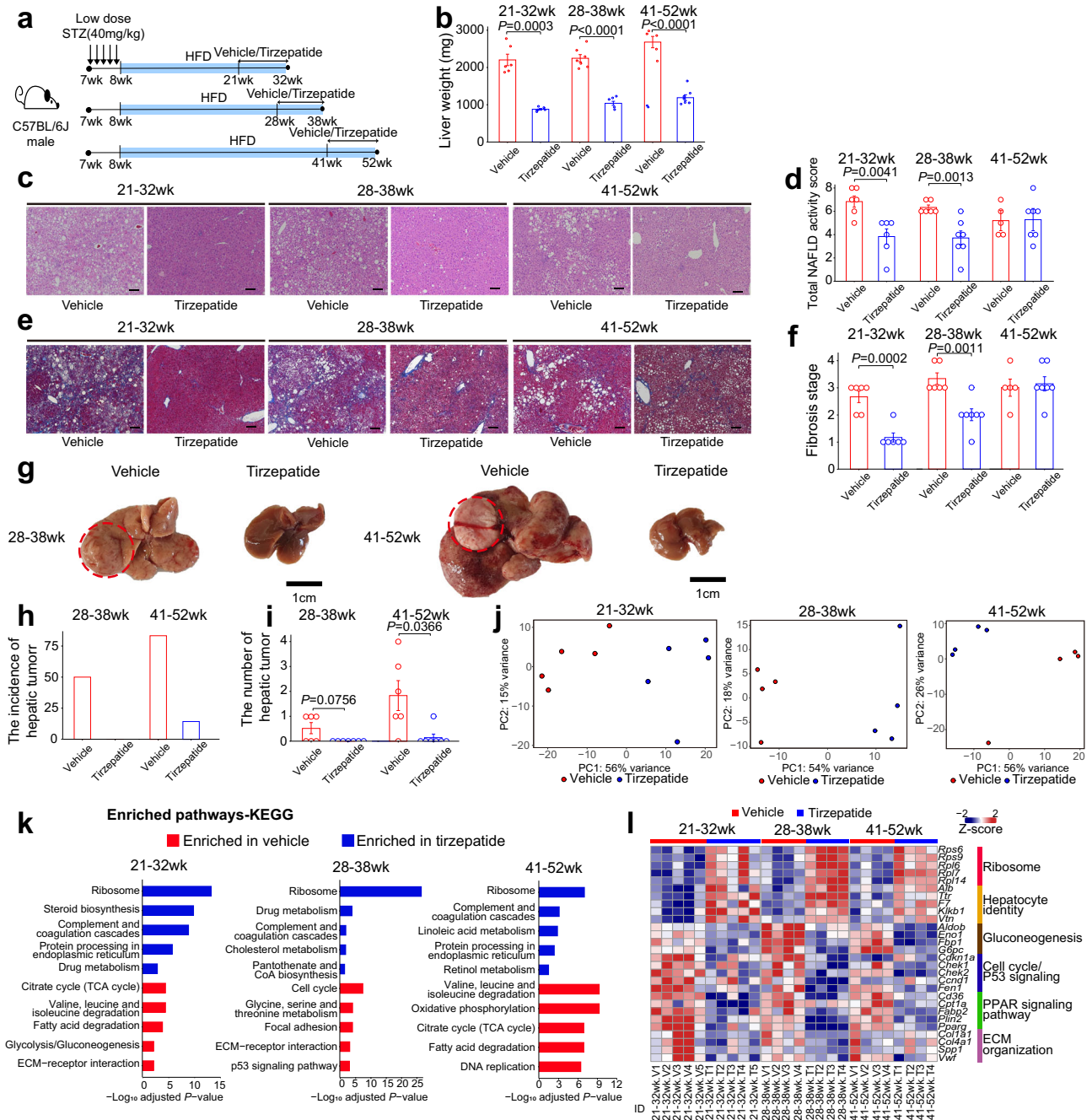


Fig. 5 | Tirzepatide ameliorates MASH, hepatic fibrosis, and hepatic tumorigenesis in STZ + HFD mice. **a–i** Seven-week-old B6J mice were treated with STZ, fed HFD from 8 weeks onwards, and administered vehicle or tirzepatide for 10–11 weeks from 21, 28, or 41 weeks of age. **a** Schematic illustration. **b** Liver weight; Vehicle, $n = 6, 7,$ and $5,$ from 21–32 to 41–52 weeks, respectively; Tirzepatide, $n = 6, 7,$ and $7,$ from 21–32 to 41–52 weeks, respectively. **c** Representative liver histology based on H&E staining (Scale bar, 100 μ m). **d** NAFLD activity score grading using the NASH CRN scoring system; Vehicle, $n = 6, 6,$ and $5,$ from 21–32 to 41–52 weeks, respectively; Tirzepatide, $n = 6, 7,$ and $7,$ from 21–32 to 41–52 weeks, respectively. **e** Representative liver histology determined via Masson’s trichrome staining (Scale bar, 100 μ m). **f** Fibrosis stage grading using the NASH CRN scoring system; Vehicle, $n = 6, 6,$ and $5,$ from 21–32 to 41–52 weeks, respectively; Tirzepatide, $n = 6, 7,$ and $7,$

from 21–32 to 41–52 weeks, respectively. **g** Representative liver gross images from STZ + HFD mice treated with vehicle or tirzepatide at 28–38 or 41–52 weeks of age (Scale bar, 1 cm). Hepatic tumor (**h**) incidence and (**i**) number of STZ + HFD mice treated with vehicle or tirzepatide at 28–38 or 41–52 weeks of age; Vehicle, $n = 6$ per group; Tirzepatide, $n = 7$ per group. **j** Principal component analyses of RNA-seq data. **k** Functional enrichment analyses using KEGG pathways for differentially expressed genes between age-matched groups subjected to tirzepatide treatment and **l** heatmap displaying the top enriched genes. Benjamini-Hochberg method and Fisher’s exact test were used. Data are expressed as means \pm SEM. $^*P < 0.05,$ $^{**}P < 0.01,$ $^{***}P < 0.001,$ $^{****}P < 0.0001,$ compared with age-matched group, two-sided Student’s t -test or Welch’s t -test (**b, d, f, i**). Source data are provided as a Source Data file.

signaling, such as *Fam53b*, *Src*, and *Sulf2*, in all stages (21–32 wk, 28–38 wk, and 41–52 wk) (Supplementary Fig. 11a–f). In contrast to the dietary change from HFD to SCD, tirzepatide treatment not only reduced body weight but also improved glycemic control along with the

improvement of hepatic phenotypes at all stages (Supplementary Fig. 10d–f). Taken together, our results suggest that tirzepatide could effectively ameliorate the development of MASH, hepatic fibrosis, and hepatic tumorigenesis in STZ + HFD mice.

Discussion

In this study, we established a murine MASLD model with histopathological characteristics encompassing the full spectrum of MASLD using low-dose STZ and HFD. Notably, from 32 weeks of age, STZ + HFD mice developed MASH and significant fibrosis. At 38 weeks, some of STZ + HFD mice developed HCC which was observed in all mice up to 68 weeks. The transcriptomic features of our model closely reflected those of MASH and MASLD-related HCC in patients. Furthermore, we demonstrated that interventions at various stages of MASLD using dietary changes or tirzepatide treatment improved MASH, hepatic fibrosis, and hepatic tumorigenesis.

The coexistence of metabolic dysfunction with the whole spectrum of MASLD, observed in the clinical setting in patients³¹, is a distinguishing feature of our animal model. STZ + HFD mice showed body weight gain and metabolic dysfunction including increased fat mass, insulin resistance, dyslipidemia, and visceral adipocyte hypertrophy and inflammation. Previous MASLD models based on STZ and HFD had limitations in that they did not show the whole spectrum of MASLD or metabolic dysfunction^{32,33}. In one study, mice were fed HFD for 15 weeks and then administered STZ at a dose of 65 mg/kg for two consecutive days³². The study found that hepatic fibrosis was increased in the group that received both HFD and STZ compared to those administered HFD or STZ only, but advanced fibrosis or MASLD-related HCC was not induced. In another study, 200 µg STZ was administered to mice two days after birth, and HFD was provided from 4 weeks of age (STAM mice)³³. Although STAM mice showed rapid MASH progression and HCC, they lacked the characteristics of metabolic dysfunction, such as obesity and insulin resistance. STAM mice developed microvesicular steatosis and mild zone 3 perivenular/pericellular fibrosis but no ballooning, indicating that the model does not mimic MASH in patients³⁴. Furthermore, the extent to which STZ and HFD contributed to the rapid progression of MASH and development of MASLD-related HCC in STAM mice is unclear, since this study did not include a control group that received STZ injections during the neonatal period but was not administered HFD.

The current STZ + HFD mouse model was characterized by metabolic dysfunction similar to severe T2DM^{35–37}. In terms of MASH histopathology, the STZ + HFD model presented hepatocyte ballooning as well as hepatic fibrosis dominant in zone 3, which is typically observed in MASH patients³⁴. In our experiments, neither MASH progression nor HCC development was observed in STZ + SCD mice. These findings imply that rapid MASH progression in our model does not occur solely as a result of STZ-induced direct toxic effects^{38,39} or hyperglycemia. Instead, prolonged metabolic stress caused by HFD is essential for the progression of MASH and development of HCC.

Beyond histopathologic and metabolic characteristics, hepatic transcriptome changes in our STZ + HFD model also precisely recapitulated the entire MASLD spectrum in patients. Similarities were identified between STZ + HFD mice at 14 to 20 weeks of age and early-stage MASH patients (NAS 2–6 and fibrosis stage 0–1), between STZ + HFD mice at 32 weeks of age and late-stage MASH patients (NAS 4–7 and fibrosis stage 4), and between HCC occurring in STZ + HFD mice and MASLD-related HCC patients. In addition, we observed a strong transcriptomic correlation between STZ + HFD mice and MASH patients with both obesity and diabetes compared to those with obesity but without diabetes. Our results demonstrated that each stage shared transcriptomic characteristics with the hepatic transcriptome of MASLD in patients. These findings support the utility of the STZ + HFD mouse model as a valuable tool for investigating the underlying pathophysiological mechanisms and development of therapeutic strategies for MASLD.

MASLD patients with obesity and T2DM show rapid MASH progression frequently accompanied by severe fibrosis^{11,12}, making them a

target population for lifestyle intervention-based pharmacological treatments¹³. While tirzepatide is an effective treatment for T2DM and obesity^{14–16} with significant promise as a therapeutic option for MASLD¹⁷, its potential long-term benefits in preventing the progression to advanced fibrosis or HCC are unknown. Since MASLD is associated with metabolic dysfunction in our model, it provides a suitable platform to examine the above issues. In this study, we validated the therapeutic efficacy of tirzepatide against MASLD. Tirzepatide attenuated MASH and fibrosis when administered in the early stage and improved fibrosis and prevented hepatic tumorigenesis when administered in the middle stage of MASH. However, administration of tirzepatide after advanced fibrosis did not improve MASH or fibrosis, only reducing hepatic tumorigenesis. These results suggest that the most appropriate time to initiate pharmacological treatment for MASLD is prior to the onset of advanced fibrosis. Intriguingly, when administered after the onset of advanced fibrosis, tirzepatide only improved HCC without effect on MASH or fibrosis. Tirzepatide downregulated the expression of genes related to the Wnt signaling pathway which is associated with HCC development in various liver diseases⁴⁰. Therefore, improving metabolic dysfunction with tirzepatide may prevent hepatic tumorigenesis regardless of changes in MASH or hepatic fibrosis by limiting metabolic reprogramming and inhibiting Wnt signaling pathway during tumor development⁴¹. Overall, our findings support the potential of tirzepatide as an effective therapeutic approach for the management of the whole spectrum of MASLD.

MASLD progression^{42,43} and MASLD-related HCC development^{44,45} have been linked to susceptibility to oxidative cellular damage. To examine the underlying cause of rapid MASH progression in our MASLD model, we compared the histopathologic, transcriptomic, and epigenetic phenotypes of four groups of mice (SCD-only, STZ + SCD, HFD-only, and STZ + HFD) at 20 weeks of age. Compared to the HFD-only group, STZ + HFD mice showed greater NAS, downregulation of genes linked to the tissue repair response, and epigenetic repression of genes related to the DNA damage response. These findings imply that a decrease in compensatory responses to metabolic stress may contribute to the rapid progression of MASH in STZ + HFD mice. Furthermore, oxidative cellular damage is known to play a significant role in the development of MASLD-related HCC⁴⁵ which could explain why HCC is frequently observed in our model. However, since additional factors, such as genomic instability, contribute to the occurrence of HCC²⁸, further research on the underlying cause of HCC development in STZ + HFD mice is warranted.

In conclusion, using low-dose STZ and HFD, we successfully established a murine MASLD model exhibiting the full spectrum of histopathologic, transcriptomic, and metabolic characteristics. With the aid of this model, we demonstrated the potential of tirzepatide as an effective therapeutic agent for MASLD. The collective findings indicate that the STZ + HFD murine model established in this study shows promise as a useful tool for advancing our knowledge of the pathophysiology of MASLD and developing innovative therapeutic options.

Methods

Animals and models

Male C57BL/6J mice purchased from Charles River Japan (Yokohama, Japan) were housed in climate-controlled, specific pathogen-free barrier facilities under a 12 h light-dark cycle at 24 °C with 40–60% humidity, and provided diet and water *ad libitum*. Because MASLD and HCC are more prevalent in males in both humans and mice, this study exclusively used male mice to ensure faster disease progression and more accurate evaluation. To generate an animal model of MASLD, STZ (Sigma-Aldrich (Saint Louis, MO, USA) S0103) at a dose of 40 mg/kg body weight was injected intraperitoneally for five consecutive days from 7 weeks of age. Mice were fed SCD

(Teklad Global 18% Protein Rodent Diet 2018; Harlan Teklad, WI, USA), 18% fat (STZ + SCD) or HFD (Research Diet (New Brunswick, NJ, USA) D12492, 60% fat) (STZ + HFD) from 8 weeks of age. Liver histology, transcriptomes, and metabolic phenotypes were assessed at multiple time-points. The dietary modification study was performed on mice in the STZ + HFD group at 20 weeks of age that were switched to SCD for 6 weeks and mice in the STZ + HFD group at 33 weeks switched to SCD for 18 weeks.

For *in vivo* efficacy studies on tirzepatide, STZ + HFD mice at 21, 28, and 41 weeks of age were randomized according to body weight. All experimental groups contained more than 6 mice. Tirzepatide was synthesized at CPC (Chinese Peptide Company, Hangzhou, China) by using the solid phase peptide synthesis method. Vehicle (HyClone DPBS, Cytiva, Germany) or tirzepatide (109.5 nmol/kg, CPC) dissolved in the vehicle was administered via subcutaneous injection to *ad libitum*-fed STZ + HFD mice 1–2 hours prior to the onset of the dark cycle every 2 days for 10 to 11 weeks. Body weights were measured every week throughout the study. The general condition of animals was monitored in all studies and no adverse effects were reported.

Human study cohort

Human liver biopsy specimens were obtained at the Severance Hospital from four healthy living donors for liver transplantation, as well as from 28 patients diagnosed with MASLD, identified by the presence of hepatic steatosis in the biopsy along with at least one of five cardiometabolic risk factors outlined in the Delphi consensus statement¹. Patients were grouped according to NAS ranging from 2 to 7 and fibrosis stages ranging from 1 to 4. Participants were excluded from the study in cases of significant alcohol intake (>30 g/day for men and 20 g/day for women) or laboratory evidence of the coexistence of other forms of liver disease with MASLD. Since our goal was to confirm the similarity between the STZ + HFD mouse model and humans in MASLD progression, we did not analyze gender differences. Participants' biological sex was self-reported.

Histological analysis

Mouse liver and epididymal white adipose tissue (eWAT) were harvested, fixed in 10% neutral buffered formalin solution (Sigma-Aldrich, Saint Louis, MO, USA), and embedded in paraffin. Formalin-fixed paraffin-embedded (FFPE) sections were stained with hematoxylin and eosin (H&E) for histological assessment of both human and mouse sections. Hepatic fibrosis was assessed using Masson's trichrome staining kit (Agilent Dako, AR173, Santa Clara, CA, USA). NAFLD activity score and fibrosis stage were determined by an expert pathologist according to the NASH CRN scoring system⁴⁶. Histological scoring was performed by researchers blinded to other information.

Immunohistochemistry, immunofluorescence, and special staining techniques

FFPE sections were deparaffinized, rehydrated, and boiled in 10 mM sodium citrate buffer (pH 6.0) for 10 minutes for antigen retrieval. Next, sections were incubated with primary antibodies against GPC-3 (Cell Marque, Rocklin, CA, USA; 261M-9, 1G12, 1:100) and GS (Merck, Darmstadt, Germany; MAB302, GS-6, 1:100) for immunohistochemical analysis. Terminal deoxynucleotidyl transferase dUTP nick end labeling (TUNEL) staining was performed after immunofluorescence staining according to the manufacturer's instructions (Roche, Basel, Switzerland; 11684795910). The number of apoptotic cells was manually counted at 20x magnification with 10 fields per case. Reticulin was stained with a Reticulum II staining kit (Roche) without dilution according to manufacturer's instructions. Images were obtained using a fluorescence or a bright-field microscope with DS-Ri2 camera (Nikon, Tokyo, Japan).

Blood chemistry analysis

Blood samples were collected by retro-orbital bleeding into plasma separation tubes with lithium heparin (BD Biosciences, Franklin Lakes, NJ, USA), followed by centrifugation at 12,000 × *g* for 1 min at 4 °C. Enzymatic colorimetric assay kits for AST (Roche), ALT (Roche), total cholesterol (Roche), TG (Roche), and free fatty acid (Wako, Osaka, Japan) were used to determine plasma levels on a Cobas 8000 modular analyzer (Roche) at GreenCross LabCell (Yongin, Korea). To examine fasting blood glucose and insulin levels, mice were fasted for 6 hours a day. Glucose concentrations were measured from the tail vein blood using a Gluco DR TOP glucometer. Peripheral blood was collected from mouse tail vein using a heparin-coated capillary tube into plasma separation tubes with lithium heparin (BD Biosciences), followed by centrifugation at 12,000 × *g* for 1 min at 4 °C. Plasma insulin concentrations were quantified using a Mouse Ultrasensitive Insulin ELISA kit (ALPCO, Salem, NH, USA) according to the manufacturer's instructions.

Glucose tolerance test

For the glucose tolerance test, 2 g per kg body weight D-glucose (Merck) in phosphate-buffered saline (PBS) was intraperitoneally injected into overnight fasted mice. Glucose concentrations were measured in tail vein blood immediately before and 15, 30, 60, 90, and 120 minutes after injection using a Gluco DR TOP glucometer (Allmedicus, Anyang, Korea).

Intravital liver imaging

To visualize hepatic lipid droplets and collagen fibers of STZ + HFD mice *in vivo*, a customized laser scanning two-photon microscopy system was used as described previously⁴⁷. In brief, intravenous injection of SF44 (120 L of 1.67 mM; SPARK Biopharma, Seoul, Korea) was used for fluorescent labeling of hepatic lipid droplets *in vivo* 30 minutes prior to imaging⁴⁸, while hepatic collagen fibers were labeled using two-photon excitation fluorescence and second harmonic generation imaging⁴⁹. In total, 4–5 mice were analyzed for each experimental group.

RNA-seq library construction and sequencing

Total RNA was isolated using a RNeasy Mini kit (Qiagen, Hilden, Germany; 74104) in keeping with the manufacturer's instructions. The integrity of total RNA was assessed using an Agilent 2100 Bioanalyzer System (Agilent Technologies, Santa Clara, CA, USA) and an Agilent RNA 6000 Nano Kit (Agilent Technologies, 5067-1511). Samples with RNA Integrity Number (RIN) values > 8 were selected for experimental use. Libraries were constructed using 1 µg total RNA. The RNA sequencing library was prepared using a NEBNext Ultra II Directional RNA Library Prep Kit for Illumina (New England BioLabs, Ipswich, MA, USA; E7760) and sequencing was performed using an Illumina Nova-Seq 6000 platform (Illumina, San Diego, CA, USA) to generate 100 bp paired-end reads.

ATAC-seq library construction and sequencing

ATAC-seq libraries were prepared from 5 mg of fresh liver tissue. In brief, nuclei were extracted using the Singulator 100 system (S2 Genomics, CA, USA) with an extended nuclear dissociation protocol. Nuclear concentrations were determined using a LUNA-FL™ Automated Fluorescence Cell Counter (Logos biosystems, Anyang, Korea) and morphological examinations were performed. Next, 50,000 nuclei were transferred to an Eppendorf tube containing 1 mL of ATAC-seq resuspension buffer (RSB; 10 mM Tris-HCl pH7.4, 10 mM NaCl, and 3 mM MgCl₂ in water) with 0.1% Tween-20. The solution was centrifuged at 500 *g* for 10 minutes at 4 °C and the supernatant removed. The pre-mixed transposition solution (25 µL 2x TD buffer from the Illumina Nextera DNA library preparation kit, 2.5 µL transposase, 16.5 µL PBS, 0.5 µL digitonin, 0.5 µL 10% Tween-20, 5 µL water) was

added to pellets, mixed by pipetting, and incubated at 37 °C for 30 minutes. Eluted DNA was purified using a Qiagen MinElute PCR purification Kit (Qiagen) and amplified with a transposed DNA fragment using the Nextera DNA Flex kit (Illumina). Quantification of DNA was performed with the PicoGreen method using Victor 3 fluorometry (cat. P7589; Invitrogen, MA, USA). The quality of ATAC-seq libraries was examined using TapeStation D1000 (Agilent) and libraries were sequenced using the HiSeq10 platform (Illumina).

Processing and analysis of RNA-seq data

Raw sequencing data obtained from mouse were mapped to mouse genome build mm10 (GRCm38) and those from humans mapped to human genome build 38 (GRCh38) using STAR (version 020201). Count matrices were generated using RSEM (v1.3.1)^{50,51}. Differential expression analysis between two groups (at least three biological replicates per condition) was performed using the DESeq2 R package (v.1.32.0) and that among multiple groups was performed using the same package with the likelihood ratio test⁵². DEGs with adjusted *p*-values less than 0.05 were used for analyses between two groups while analyses of more than three groups used DEGs with adjusted *p*-value less than 0.001. DEGs were subjected to *k*-means clustering with R stats package (v.4.2.2) using the optimal number of clusters. The optimal number of clusters was determined with the *fviz_nbclust*() function using the Factoextra R package (v.1.0.7). Functional enrichment analyses of genes were performed with Enrichr (v.3.2) using KEGG_2019_Mouse and GO_Biological_Process_2021 gene-set libraries^{53,54}. Correlation analysis of mouse and human global transcriptome was conducted using SubMap version 4, which is Subclass Mapping algorithm implemented in the GenePattern genomic analysis toolkit, with default settings and the resulting nominal *p*-values with Fisher's exact test used⁵⁵. To identify the transcriptomic changes shared between mouse and human systems, genes that were differentially expressed in same direction in both species were collected and integrated with high-confidence interactions from STRING (v.11.0) to generate a protein interaction network (edge score, >0.7)⁵⁶. The generated network was inputted into the CDAPS hierarchical clustering tool using the OSLOM clustering algorithm in Cytoscape (v.3.10.1)^{57–59}. The resulting gene cluster system of highly interconnected genes was annotated with KEGG, GO and REACTOME pathway databases using *g:Profiler* from the 2023-04-19 release⁶⁰. The list of genes involved in the Wnt signaling pathway was referenced using Gene Ontology data (GO:0016055) from the 2024-03-28 release^{61,62}. Gene set enrichment analyses were performed with GSEA v.4.3.3 using human HCC signature gene sets from three published data^{25–27,63}.

Processing and analysis of ATAC-seq data

Raw ATAC-seq data were trimmed by removing adapters and sequences shorter than 36 base pairs (bp) using TrimGalore (ver. 0.5.0)⁶⁴. The quality of processed reads was assessed using FastQC. All trimmed data had >90% ratio of reads with Phred quality scores of over 30⁶⁵. Trimmed data were aligned to the mouse genome (mm10, GRCm38) using Bowtie2 (version 2.3.5.1) using the following parameters: *-very-sensitive -no-discordant -no-mixed -no-unal*⁶⁶. Mitochondrial reads were subsequently removed using Samtools (version 1.9) and PCR duplicated reads removed using Picard MarkDuplicates tool (Picard version 2.2.2)^{67,68}. Peak calling was performed with MACS2 (version 2.1.1) and ENCODE blacklisted regions for mm10 subtracted with Bedtools intersect (version 2.27.1)^{69,70}.

Differentially accessible regions between groups were identified using Diffbind (v.3.4.11) within R⁷¹. In brief, peaks from MACS2 and sample metadata were inputted into R, and read counts for consensus peaksets and overlapping peaks in each sample

subsequently counted. Counts were normalized and the Pearson Correlation Coefficient between each sample was calculated using the R *cor.test*() function. Differentially accessible regions (peaks) between each group were examined with DESeq2 (adjusted *p*-value < 0.05)⁵². The differentially accessible regions for each comparison analysis were divided into two groups based on fold change (upregulated or downregulated) and overlapping genes annotated using annotation databases (TxDb.Mmusculus.UCSC.mm10.knownGene). Functional enrichment analysis of genes was performed with Enrichr as described above.

Statistical analysis and reproducibility

All results are expressed as mean ± standard error of the mean. Levene's test of equality of variances was used to examine homogeneity of variance across groups. Then comparisons of groups with homogeneity of variance were performed using two-tailed Student's *t*-test or analysis of variance with post-hoc Tukey's test. On the other hand, comparisons of groups without homogeneity of variance were performed using Welch's *t*-test or Welch's analysis of variance with post-hoc Games-Howell test. Fisher's exact test was used to verify the association between categorical variables. *P* values below 0.05 were considered statistically significant. All analyses were performed using R package stats (ver. 4.2.2) and rstatix (ver. 0.7.2).

To choose the sample size for experiments, the effect size of the NAFLD activity score between the 20-week-old STZ + HFD mice and the control mice before STZ treatment was calculated. The result was 3.38 (Cohen's *d*). Based on this effect size, a sample size of 2.75 was required to detect a difference with a *p*-value of 0.05 and a power of 0.80 between the two groups. In vivo imaging and sequencing studies were then carried out with at least 3 biological replicates each. All data were included in the analysis except for cases where mice died unexpectedly during the experiment. All mice were randomly assigned to their respective groups. The NAFLD activity scores and fibrosis stages were evaluated in a blinded fashion. The investigators were blinded to group allocation during data collection and analysis.

Reporting summary

Further information on research design is available in the Nature Portfolio Reporting Summary linked to this article.

Data availability

The RNA-seq and ATAC-seq data generated in this study have been deposited in the Gene Expression Omnibus (GEO) database under the accession code [GSE246223](https://www.ncbi.nlm.nih.gov/geo/query/acc.cgi?acc=GSE246223). Expression dataset of NAFLD patients with obesity, NAFLD patients with HCC, and HCC patients with other etiologies were downloaded from GEO database ([GSE163211](https://www.ncbi.nlm.nih.gov/geo/query/acc.cgi?acc=GSE163211), [GSE164760](https://www.ncbi.nlm.nih.gov/geo/query/acc.cgi?acc=GSE164760), [GSE63898](https://www.ncbi.nlm.nih.gov/geo/query/acc.cgi?acc=GSE63898)). The RNA-seq data of diethylnitrosamine-treated HFD-fed mice was downloaded from the Genome Sequence Archive [<https://ngdc.cncb.ac.cn/gsa/browse/CRA000931>]. Molecular signature gene sets of HCCs were obtained from three publicly available data [<https://doi.org/10.1002/hep.21467>], [<https://doi.org/10.1158/0008-5472.CAN-09-1089>], [<https://doi.org/10.1002/hep.29254>]]. Source data are provided with this paper.

References

1. Rinella, M. E. et al. A multisociety Delphi consensus statement on new fatty liver disease nomenclature. *J. Hepatol.* **79**, 1542–1556 (2023).
2. Powell, E. E., Wong, V. W. S. & Rinella, M. Non-alcoholic fatty liver disease. *Lancet* **397**, 2212–2224 (2021).
3. Teng, M. L. et al. Global incidence and prevalence of nonalcoholic fatty liver disease. *Clin. Mol. Hepatol.* **29**, S32–S42 (2023).

4. Younossi, Z. M. et al. The economic and clinical burden of non-alcoholic fatty liver disease in the United States and Europe. *Hepatology* **64**, 1577–1586 (2016).
5. Huang, D. Q., El-Serag, H. B. & Loomba, R. Global epidemiology of NAFLD-related HCC: trends, predictions, risk factors and prevention. *Nat. Rev. Gastroenterol. Hepatol.* **18**, 223–238 (2021).
6. Schattenberg, J. M. et al. Disease burden and economic impact of diagnosed non-alcoholic steatohepatitis in five European countries in 2018: A cost-of-illness analysis. *Liver Int.* **41**, 1227–1242 (2021).
7. Febbraio, M. A. et al. Preclinical models for studying NASH-driven HCC: How useful are they? *Cell Metab.* **29**, 18–26 (2019).
8. Younossi, Z. M. et al. The global epidemiology of NAFLD and NASH in patients with type 2 diabetes: A systematic review and meta-analysis. *J. Hepatol.* **71**, 793–801 (2019).
9. Kanwal, F. et al. Effect of metabolic traits on the risk of cirrhosis and hepatocellular cancer in nonalcoholic fatty liver disease. *Hepatology* **71**, 808–819 (2020).
10. Jarvis, H. et al. Metabolic risk factors and incident advanced liver disease in non-alcoholic fatty liver disease (NAFLD): A systematic review and meta-analysis of population-based observational studies. *PLoS Med.* **17**, e1003100 (2020).
11. Castera, L. et al. High prevalence of NASH and advanced fibrosis in Type 2 Diabetes: A prospective study of 330 outpatients undergoing liver biopsies for elevated ALT, using a low threshold. *Diab. Care* **46**, 1354–1362 (2023).
12. Ajmera, V. et al. A prospective study on the prevalence of NAFLD, advanced fibrosis, cirrhosis and hepatocellular carcinoma in people with type 2 diabetes. *J. Hepatol.* **78**, 471–478 (2023).
13. Rinella, M. E. et al. AASLD Practice Guidance on the clinical assessment and management of nonalcoholic fatty liver disease. *Hepatology* **77**, 1797–1835 (2023).
14. Frias, J. P. et al. Tirzepatide versus Semaglutide once weekly in patients with Type 2 diabetes. *N. Engl. J. Med.* **385**, 503–515 (2021).
15. Garvey, W. T. et al. Tirzepatide once weekly for the treatment of obesity in people with type 2 diabetes (SURMOUNT-2): a double-blind, randomised, multicentre, placebo-controlled, phase 3 trial. *Lancet* **402**, 613–626 (2023).
16. Jastreboff, A. M. et al. Tirzepatide once weekly for the treatment of obesity. *N. Engl. J. Med.* **387**, 205–216 (2022).
17. Gastaldelli, A. et al. Effect of tirzepatide versus insulin degludec on liver fat content and abdominal adipose tissue in people with type 2 diabetes (SURPASS-3 MRI): a substudy of the randomised, open-label, parallel-group, phase 3 SURPASS-3 trial. *Lancet Diab. Endocrinol.* **10**, 393–406 (2022).
18. Watt, M. J., Miotto, P. M., De Nardo, W. & Montgomery, M. K. The Liver as an Endocrine Organ - Linking NAFLD and Insulin Resistance. *Endocr. Rev.* **40**, 1367–1393 (2019).
19. Subudhi, S. et al. Distinct hepatic gene-expression patterns of NAFLD in patients with obesity. *Hepatol. Commun.* **6**, 77–89 (2022).
20. Olofson, A. M., Gonzalo, D. H., Chang, M. & Liu, X. Steatohepatitic variant of hepatocellular carcinoma: a focused review. *Gastroenterol. Res.* **11**, 391–396 (2018).
21. Salomao, M., Yu, W. M., Brown, R. S., Emond, J. C. & Lefkowitz, J. H. Steatohepatitic hepatocellular carcinoma (SH-HCC): A distinctive histological variant of HCC in hepatitis C virus-related cirrhosis with associated NAFLD/NASH. *Am. J. Surg. Pathol.* **34**, 1630–1636 (2010).
22. Takahashi, Y. Histopathology of nonalcoholic fatty liver disease/nonalcoholic steatohepatitis. *World J. Gastroenterol.* **20**, 15539 (2014).
23. Schlageter, M., Terracciano, L. M., D'Angelo, S. & Sorrentino, P. Histopathology of hepatocellular carcinoma. *World J. Gastroenterol.* **20**, 15955 (2014).
24. Yao, S. et al. Diagnostic value of immunohistochemical staining of GP73, GPC3, DCP, CD34, CD31, and Reticulin staining in Hepatocellular Carcinoma. *J. Histochem. Cytochem.* **61**, 639–648 (2013).
25. Désert, R. et al. Human hepatocellular carcinomas with a periportal phenotype have the lowest potential for early recurrence after curative resection. *Hepatology* **66**, 1502–1518 (2017).
26. Hoshida, Y. et al. Integrative transcriptome analysis reveals common molecular subclasses of human hepatocellular carcinoma. *Cancer Res.* **69**, 7385–7392 (2009).
27. Boyault, S. et al. Transcriptome classification of HCC is related to gene alterations and to new therapeutic targets. *Hepatology* **45**, 42–52 (2007).
28. Pinyol, R. et al. Molecular characterisation of hepatocellular carcinoma in patients with non-alcoholic steatohepatitis. *J. Hepatol.* **75**, 865–878 (2021).
29. Villanueva, A. et al. DNA methylation-based prognosis and epigenetic drivers in hepatocellular carcinoma. *Hepatology* **61**, 1945–1956 (2015).
30. Wang, Q. et al. Time serial transcriptome reveals Cyp2c29 as a key gene in hepatocellular carcinoma development. *Cancer Biol. Med* **17**, 401–417 (2020).
31. Cariou, B., Byrne, C. D., Loomba, R. & Sanyal, A. J. Nonalcoholic fatty liver disease as a metabolic disease in humans: A literature review. *Diab. Obes. Metab.* **23**, 1069–1083 (2021).
32. Lo, L. et al. Diabetes is a progression factor for hepatic fibrosis in a high fat fed mouse obesity model of non-alcoholic steatohepatitis. *J. Hepatol.* **55**, 435–444 (2011).
33. Fujii, M. et al. A murine model for non-alcoholic steatohepatitis showing evidence of association between diabetes and hepatocellular carcinoma. *Med Mol. Morphol.* **46**, 141–152 (2013).
34. Farrell, G. et al. Mouse models of nonalcoholic steatohepatitis: toward optimization of their relevance to human nonalcoholic steatohepatitis. *Hepatology* **69**, 2241–2257 (2019).
35. Zhang, M., Lv, X. Y., Li, J., Xu, Z. G. & Chen, L. The characterization of high-fat diet and multiple low-dose streptozotocin induced type 2 diabetes rat model. *Exp. Diab. Res* **2008**, 704045 (2008).
36. Srinivasan, K., Viswanad, B., Asrat, L., Kaul, C. L. & Ramarao, P. Combination of high-fat diet-fed and low-dose streptozotocin-treated rat: A model for type 2 diabetes and pharmacological screening. *Pharm. Res* **52**, 313–320 (2005).
37. Reed, M. J. et al. A new rat model of type 2 diabetes: The fat-fed, streptozotocin-treated rat. *Metabolism* **49**, 1390–1394 (2000).
38. Imaeda, A., Kaneko, T., Aoki, T., Kondo, Y. & Nagase, H. DNA damage and the effect of antioxidants in streptozotocin-treated mice. *Food Chem. Toxicol.* **40**, 979–987 (2002).
39. Kume, E. et al. Morphological and gene expression analysis in mouse primary cultured hepatocytes exposed to streptozotocin. *Exp. Toxicol. Pathol.* **56**, 245–253 (2005).
40. Zou, G. & Park, J. I. Wnt signaling in liver regeneration, disease, and cancer. *Clin. Mol. Hepatol.* **29**, 33–50 (2023).
41. Du, D. et al. Metabolic dysregulation and emerging therapeutic targets for hepatocellular carcinoma. *Acta Pharm. Sin. B* **12**, 558–580 (2022).
42. Seki, S. et al. In situ detection of lipid peroxidation and oxidative DNA damage in non-alcoholic fatty liver diseases. *J. Hepatol.* **37**, 56–62 (2002).
43. Schults, M. A. et al. Decreased nucleotide excision repair in steatotic livers associates with myeloperoxidase-immunoreactivity. *Mutat. Res. - Fundam. Mol. Mech. Mutagen.* **736**, 75–81 (2012).
44. Tanaka, S. et al. Increased hepatic oxidative DNA damage in patients with nonalcoholic steatohepatitis who develop hepatocellular carcinoma. *J. Gastroenterol.* **48**, 1249–1258 (2013).
45. Brahma, M. K. et al. Oxidative stress in obesity-associated hepatocellular carcinoma: sources, signaling and therapeutic challenges. *Oncogene* **40**, 5155–5167 (2021).

46. Kleiner, D. E. et al. Design and validation of a histological scoring system for nonalcoholic fatty liver disease. *Hepatology* **41**, 1313–1321 (2005).
47. Moon, J. et al. Intravital two-photon imaging and quantification of hepatic steatosis and fibrosis in a live small animal model. *Biomed. Opt. Express* **12**, 7918 (2021).
48. Kim, E., Lee, S. & Park, S. B. A Seoul-Fluor-based bioprobe for lipid droplets and its application in image-based high throughput screening. *Chem. Commun.* **48**, 2331 (2012).
49. Sun, W. et al. Nonlinear optical microscopy: use of second harmonic generation and two-photon microscopy for automated quantitative liver fibrosis studies. *J. Biomed. Opt.* **13**, 064010 (2008).
50. Dobin, A. et al. STAR: Ultrafast universal RNA-seq aligner. *Bioinformatics* **29**, 15–21 (2013).
51. Li, B. & Dewey, C. N. RSEM: Accurate transcript quantification from RNA-Seq data with or without a reference genome. *BMC Bioinforma.* **12**, 323 (2011).
52. Love, M. I., Huber, W. & Anders, S. Moderated estimation of fold change and dispersion for RNA-seq data with DESeq2. *Genome Biol.* **15**, 550 (2014).
53. Kuleshov, M. V. et al. Enrichr: a comprehensive gene set enrichment analysis web server 2016 update. *Nucleic Acids Res.* **44**, W90–W97 (2016).
54. Chen, E. Y. et al. Enrichr: Interactive and collaborative HTML5 gene list enrichment analysis tool. *BMC Bioinforma.* **14**, 128 (2013).
55. Hoshida, Y., Brunet, J. P., Tamayo, P., Golub, T. R. & Mesirov, J. P. Subclass mapping: Identifying common subtypes in independent disease data sets. *PLoS One* **2**, e1195 (2007).
56. Szklarczyk, D. et al. STRING v11: Protein-protein association networks with increased coverage, supporting functional discovery in genome-wide experimental datasets. *Nucleic Acids Res.* **47**, D607–D613 (2019).
57. Singhal, A. et al. Multiscale community detection in cytoscape. *PLoS Comput. Biol.* **16**, e1008239 (2020).
58. Lancichinetti, A., Radicchi, F., Ramasco, J. J. & Fortunato, S. Finding statistically significant communities in networks. *PLoS One* **6**, e18961 (2011).
59. Shannon, P. et al. Cytoscape: A software Environment for integrated models of biomolecular interaction networks. *Genome Res.* **13**, 2498–2504 (2003).
60. Raudvere, U. et al. G-Profiler: A web server for functional enrichment analysis and conversions of gene lists (2019 update). *Nucleic Acids Res.* **47**, W191–W198 (2019).
61. Gene Ontology, C. et al. The Gene Ontology knowledgebase in 2023. *Genetics* **224**, iyad031 (2023).
62. Ashburner, M. et al. Gene ontology: Tool for the unification of biology. *Nat. Genet.* **25**, 25–29 (2000).
63. Subramanian, A. et al. Gene set enrichment analysis: A knowledge-based approach for interpreting genome-wide expression profiles. *Proc. Natl Acad. Sci. USA* **102**, 15545–15550 (2005).
64. Krueger, F., James, F., Ewels, P., Afyounian, E. & Schuster-Boeckler, B. TrimGalore. *Babraham Bioinformatics* (2021).
65. Andrews, S. FastQC. *Babraham Bioinformatics* (2010).
66. Langmead, B. & Salzberg, S. L. Fast gapped-read alignment with Bowtie 2. *Nature Methods*. Nature Publishing Group (2012).
67. Danecek, P. et al. Twelve years of SAMtools and BCFtools. *Giga-science* **10**, giab008 (2021).
68. Institute, B. Picard toolkit. *Broad Institute, GitHub repository* (2019).
69. Quinlan, A. R. & Hall, I. M. BEDTools: A flexible suite of utilities for comparing genomic features. *Bioinformatics* **26**, 841–842 (2010).
70. Gaspar, J. M. Improved peak-calling with MACS2. *bioRxiv* (2018).
71. Stark, R. & Brown, G. DiffBind: differential binding analysis of ChIP-Seq peak data. *Bioconductor* (2011).

Acknowledgements

This research was supported by a grant of MD-PhD/Medical Scientist Training Program through the Korea Health Industry Development Institute (KHIDI), funded by the Ministry of Health & Welfare, Republic of Korea (to B-K.J. and W.H.L.), a Medical Scientist Training Program from the Ministry of Science & ICT of Korea, and grants of National Research Foundation of Korea (2021R111A1A01043936 to W-I.C.; 2021M3E5D1A02015181 to W.C.; 2021R1A2C1012480 to Y.A.M.; 2020M3A9E4039184 to J.Y.P.; and 2021R1A2C3005108, 2020M3A9E4038695 to H.K.). We thank Won Gun Choi and Inseon Hwang for their helpful discussions and technical support. We also thank Hyeon Kyu Lee, Jungsun Park, Jung Eun Nam, Hee-Saeng Jung, Ju Eun Kim, and Hwajin Kim for their technical assistance in experiments.

Author contributions

B-K.J., W-I.C., W.C., J.Y.P., and H.K. were responsible for the study concept and design. B-K.J., W-I.C., W.C., J.M., W.H.L., C.C., I.Y.C, S-H.L, J.K.K, P.K., Y.S.J., J.Y.P. and H.K. were responsible for the acquisition of data, technical and material support. B-K.J., W-I.C., W.C., W.H.L., Y.A.M. and H.K. were responsible for analysis and interpretation of data. B-K.J., W-I.C., W.C., Y.A.M, J.Y.P., and H.K. were responsible for the drafting of the manuscript. Y.S.J and J.Y.P. were responsible for critical revision of the manuscript for important intellectual content. All authors have critically reviewed the paper and approved the final version.

Competing interests

The authors declare no competing interests.

Ethics

All animal experiments complied with the relevant ethical regulations. Experimental protocols for this study were approved by the Institutional Animal Care and Use Committee of Korea Advanced Institute of Science and Technology (KAIST). The criteria for terminating the animal experiment were set as follows: if the size of the hepatic tumor measured externally in the mice exceeded a maximum diameter of 20 mm, or if the weight loss was more than 20%. Only one mouse had a tumor size that exceeded the maximum diameter, measuring 21 mm, which was within the margin of human error. Each week, the surface skin of the mouse liver was visually inspected and palpated to assess tumorigenesis, and the weight was measured to ensure compliance with these criteria. Experiments using human specimens were performed in accordance with the ethical guidelines of the 1975 Declaration of Helsinki and written informed consent was obtained from each participant. There was no compensation provided to research subjects for their participation. The study protocol was approved by the Severance Hospital Institutional Review Board (IRB No. 4-2018-0537, Seoul, Korea).

Additional information

Supplementary information The online version contains supplementary material available at <https://doi.org/10.1038/s41467-024-50660-y>.

Correspondence and requests for materials should be addressed to Wonsuk Choi, Jun Yong Park or Hail Kim.

Peer review information *Nature Communications* thanks Hidekazu Tsukamoto, and the other, anonymous, reviewer(s) for their contribution to the peer review of this work. A peer review file is available.

Reprints and permissions information is available at <http://www.nature.com/reprints>

Publisher's note Springer Nature remains neutral with regard to jurisdictional claims in published maps and institutional affiliations.

Open Access This article is licensed under a Creative Commons Attribution-NonCommercial-NoDerivatives 4.0 International License, which permits any non-commercial use, sharing, distribution and reproduction in any medium or format, as long as you give appropriate credit to the original author(s) and the source, provide a link to the Creative Commons licence, and indicate if you modified the licensed material. You do not have permission under this licence to share adapted material derived from this article or parts of it. The images or other third party material in this article are included in the article's Creative Commons licence, unless indicated otherwise in a credit line to the material. If material is not included in the article's Creative Commons licence and your intended use is not permitted by statutory regulation or exceeds the permitted use, you will need to obtain permission directly from the copyright holder. To view a copy of this licence, visit <http://creativecommons.org/licenses/by-nc-nd/4.0/>.

© The Author(s) 2024